

*Short Note*Velocity Structure of the Tibetan Lithosphere: Constraints from *P*-Wave Travel Times of Regional Earthquakes

by Jessica D. Griffin, Robert L. Nowack, Wang-Ping Chen, and Tai-Lin Tseng*

Abstract Using data from regional earthquakes recorded by the Hi-CLIMB array in Tibet, we model *P*-wave arrival times to constrain the velocity structure in the crust and the upper mantle in central and western Tibet. Of more than 30 high-quality, regional seismic profiles that have been assembled, we have selected 10 that show excellent crustal and *Pn* arrivals for further analysis. Travel times from four events along the Hi-CLIMB array provide details on crustal velocities, and six events at regional distances to the array provide further constraints on Moho structure and upper-mantle–lid velocities. We use three-dimensional ray tracing to model the travel times, and the results indicate that the Moho beneath the Lhasa terrane of southern Tibet is over 73 km deep, with a *Pn* speed of about 8.2 km/s. The Qiangtang terrane north of the Bangong–Nujiang suture (BNS) shows a thinner crust, by up to 10 km, and a lower *Pn* speed of 7.8–7.9 km/s. Travel times from events to the west and east of the array indicate that both Moho structure and mantle–lid velocities in the region are three-dimensional in nature but approximately follow the trend of the BNS. Although only a limited number of events were used for the travel-time modeling, the results are consistent with earlier results from teleseismic imaging using the Hi-CLIMB array.

Online Material: Regional earthquake locations.

Introduction

The Himalayan–Tibetan orogeny is the largest active continent–continent collision zone in the world (Yin and Harrison, 2000), and the continuing convergence has resulted in large scale deformation in central Eurasia (Molnar and Tapponnier, 1975; Tapponnier *et al.*, 2001). The Hi-CLIMB (Himalayan–Tibetan Continental Lithosphere During Mountain Building) experiment was conducted along a north–south corridor between 84° E and 86° E, extending from the Ganga foreland basin, over the Lesser and Higher Himalayas, crossing the Indus–Yarlung suture (IYS) and the Bangong–Nujiang suture (BNS), then reaching into the Qiangtang terrane in central Tibet (Fig. 1). Between 2002 and 2005, the Hi-CLIMB array was deployed in three phases, with a total of over 210 broadband sites (Nabelek *et al.*, 2005). A unique feature of the Hi-CLIMB experiment is that it crosses the highest portions of the Himalayas from the Indian shield to the interior of Tibet. It also has an important combination of a dense station spacing of 3–8 km for the main linear array and a broad regional coverage. In this study, we investigate data from the linear array

component of Hi-CLIMB in Tibet to analyze first-arrival travel times from regional earthquakes.

Because of the importance of the region for understanding active continental collision, Tibet has been the site of several large-scale field experiments in recent years (e.g., Hirn *et al.*, 1984; Zhao *et al.*, 1993; McNamara *et al.*, 1994; Kind *et al.*, 2002; Tilmann *et al.*, 2003; Wittlinger *et al.*, 2004, 2009). Studies of *Pn* in Tibet have found thicknesses of roughly double the continental average (Chen and Molnar, 1981; Hearn *et al.*, 2004; and Liang *et al.*, 2004; Liang and Song, 2006; Sun and Toksoz, 2006).

Using teleseismic data from the Hi-CLIMB experiment, the crust was found to be from 70 to 80 km thick beneath the Lhasa terrane but on the order of 10 km thinner beneath the Qiangtang terrane to the north (Nabelek *et al.*, 2009; Tseng *et al.*, 2009; Nowack *et al.*, 2010). From the analysis of wide-angle and teleseismic data from the INDEPTH III seismic array, located about 5° to the east of the Hi-CLIMB array but crossing similar terranes, a somewhat smaller change in crustal thickness was found from south to north (Zhao *et al.*, 2001; Kind *et al.*, 2002; Shi *et al.*, 2004; Tian, *et al.*, 2005). While the Moho conversion is distinct and coherent beneath

*Now at the Department of Geosciences, National Taiwan University, Taipei, Taiwan.

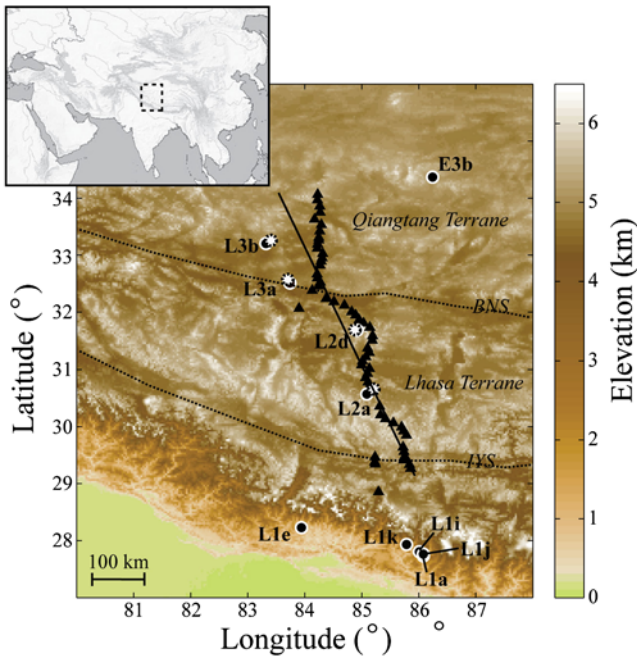


Figure 1. The topography of the Tibetan Plateau shown with the stations of the Hi-CLIMB array in Tibet (triangles) and the epicenters of the selected regional earthquake sources (circles). Black circles indicate the USGS/NEIC PDE and EHB reported hypocenters, and the white dots with dashed outlines indicate the epicenters of the four events nearest to the array, which have been relocated in this study. The locations of the Bangong–Nujiang suture (BNS) and the Indus–Yarlung suture (IYS) are shown by the dotted lines, and the solid line gives the reference line along the Hi-CLIMB array. The color version of this figure is available only in the electronic edition.

a majority of both the Lhasa and Qiangtang terranes from receiver function images of Hi-CLIMB data images, the conversion strength was observed to vary with the direction of illumination (Nabelek *et al.*, 2009; Nowack *et al.*, 2010). Also from Hi-CLIMB data, a zone of crustal and Moho disruption marks the BNS zone between the more stable Lhasa and Qiangtang blocks (Nowack *et al.*, 2010).

From travel-time studies, the average P_g velocities in the Tibetan crust were found to be lower than the continental average, in the range of 6.2–6.3 km/s (Zhao *et al.*, 2001; Monsalve *et al.*, 2008; Steck *et al.*, 2009). Studies from the Hi-CLIMB and INDEPTH experiments, which have more dense station spacings, found similar average crustal velocities. Also, lower crustal velocities were found in the areas of the IYS and the BNS for Hi-CLIMB (Hung *et al.*, 2010) and in the area of the BNS for INDEPTH III (Haines *et al.*, 2003; Meissner *et al.*, 2004).

Upper-mantle P -wave velocities beneath the Qiangtang terrane north of the BNS were found from regional travel-time studies to be as low as 7.9 km/s (Hearn *et al.*, 2004; Liang *et al.*, 2004; Pei *et al.*, 2007). These low velocities, as well as the inefficient S_n propagation observed in this area (Barazangi and Ni, 1982; Ni and Barazangi, 1983; Brandon and Romanowicz, 1986; McNamara *et al.*, 1995, 1997; Xie

et al., 2004; Barron and Priestley, 2009), imply that the thinner crust of the Qiangtang terrane is at least in part isostatically supported by an underlying mantle that is hotter and more buoyant (Zhao *et al.*, 2001; Jimenez-Munt *et al.*, 2008). The P -wave velocities inferred beneath the southern Tibetan plateau, south of the BNS, are as high as 8.3 km/s and similar to the upper-mantle velocities observed beneath stable cratonic regions, such as the Indian shield or the Tarim and Sichuan basins (McNamara *et al.*, 1997; Liang and Song, 2006; Pei *et al.*, 2007).

The differences between results from Hi-CLIMB and INDEPTH III highlight the fact that, while the Tibetan plateau is composed of a succession of terranes from north to south (Dewey *et al.*, 1988), there exists significant lateral variation from west to east, and the structure of the plateau must be taken into account in all three dimensions. In this study, forward modeling of P -wave travel times from regional earthquakes recorded by the linear array component of Hi-CLIMB in Tibet is used to determine the three-dimensional (3D) P -wave velocity structure for the region of the central and western Tibetan plateau beneath the Hi-CLIMB array.

Data Analysis

We used broadband seismic data from regional earthquakes in Tibet recorded by the densely spaced, linear component of the Hi-CLIMB array in Tibet (Fig. 1) to investigate crustal and upper-mantle structure. Based on locations of epicenters reported in the Engdahl–van der Hilst–Buland (EHB) catalog (Engdahl *et al.*, 1998; see [Data and Resources](#)) or the National Earthquake Information Center Preliminary Determination of Epicenter (NEIC PDE) catalog [U.S. Geological Survey (USGS); see [Data and Resources](#) for events not included in the EHB], we selected events for which both P_g and P_n arrivals were recorded by the Hi-CLIMB array in Tibet (Fig. 1; [ⓔ](#) a list of events is available as an electronic supplement to this paper).

To construct a velocity model along the trend of the Hi-CLIMB array in Tibet, we relied on data from four events located along and near the array (L2a, L2d, L3a, and L3b; Fig. 1) for crustal structure. In addition, we used six events whose epicenters are about 200–300 km from the nearest station to constrain seismic velocity structures in the crust and the upper mantle on a regional scale. Four of the events to the south of the array have similar epicenters, and these provide some verification on the variation in the P -wave travel times due to small-scale heterogeneity, as well as picking errors. The entire group of events was selected to be largely in line with the trend of the array but also to provide a range of azimuthal coverage. We visually picked the timing of the first P arrivals on the vertical component of the broadband seismograms after applying a six-pole, Butterworth band-pass filter between 0.5 and 5.0 Hz. The average pick error is estimated to be ± 0.3 s. Figure 2 shows examples of seismic record sections from two events, with the traces plotted with

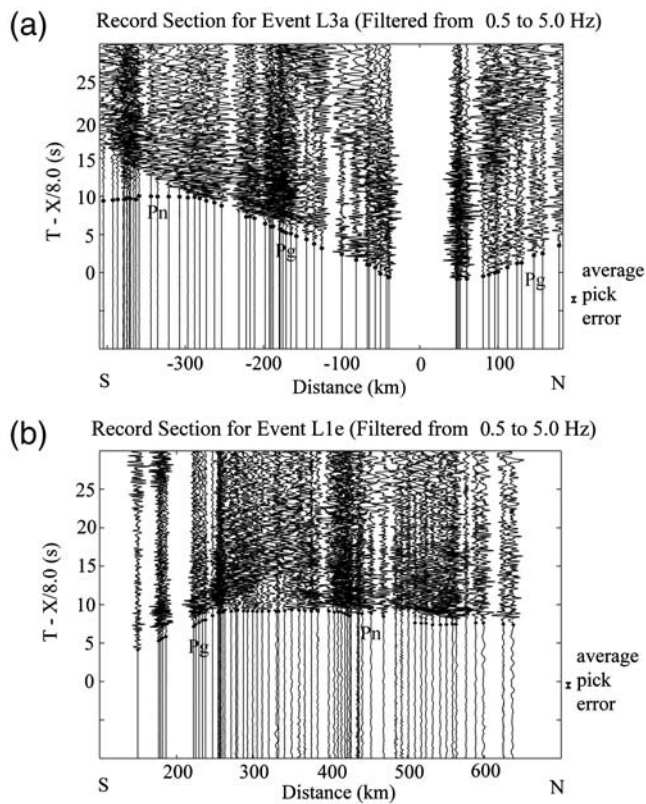


Figure 2. Examples of vertical component record section recorded by the Hi-CLIMB array in central Tibet. (a) The record section for earthquake L3a; (b) the record section for earthquake L1e. On both record sections, the first arriving P_g or P_n waves are indicated. The waveforms were filtered with a six-pole Butterworth band-pass filter between 0.5 and 5.0 Hz. The data are shown in reduced time by 8.0 km/s, and each trace is amplitude normalized. For each trace on the record sections, the first arrivals of P waves are marked by black dots.

respect to surface distance of the event to each station, and all travel times are reduced by 8.0 km/s.

We carried out forward modeling of the travel times using a 3D ray-tracing code by [Cerveny et al. \(1988\)](#); the CRT algorithm). In doing so, the elevation of the free surface in the model is at 5 km above sea-level, the average elevation of the Hi-CLIMB stations. The model consists of a grid system, with a spacing of 1° in longitude, 0.5° in latitude, and 10 km in depth, over the region between 27° and 36° N in latitude and 80° to 90° E in longitude and extending down to a depth of 200 km. The Moho is an explicit surface separating grid-points in the crust from those in the upper mantle. A scheme of cubic splines interpolate among the nodes of the grid system to specify values of seismic wave speeds and positions of the Moho and to calculate ray paths in the 3D model. An example of the 3D ray tracing for event L1e is shown in Figure 3.

Earthquake Events along the Hi-CLIMB Array

The epicenters for earthquakes L2a, L2d, L3a, and L3b are located along the length of the Hi-CLIMB array in Tibet

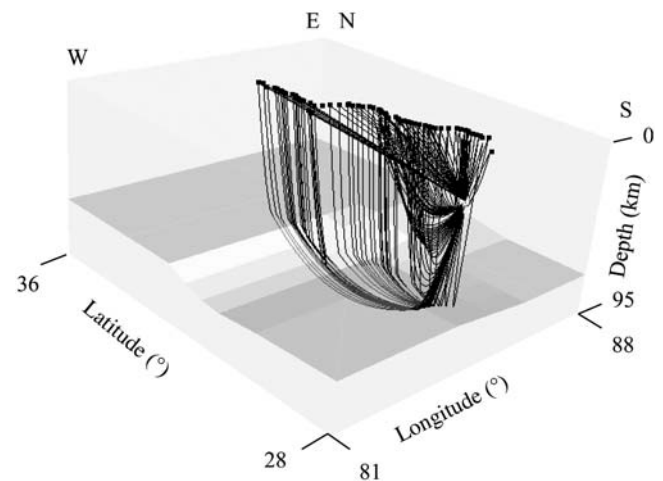


Figure 3. A rendering of the P -wave ray paths calculated by the 3D ray-tracing code CRT (black lines) for the event L1e as viewed from the west. The gray surface indicates the structure of the Moho used within the input velocity model for the ray tracing.

(Fig. 1), and the P_g travel times recorded from these nearby sources are used to constrain the crustal velocity structure beneath the array. The four events were first relocated using the location code HYPOINVERSE 2000 ([Klein, 2002](#)), and the relocated epicenters range from 4 to 15 km distant from the reported epicenters (a table of the relocated hypocenters for the nearby events is available in the electronic supplement to this paper). Also, while the reported depths of these sources are between 15 and 19 km below the surface, their depths changed to 6–15 km below the surface after relocation, which are more consistent with the shallow crustal seismogenic zone in Tibet ([Chen and Molnar, 1983](#); [De la Torre et al., 2007](#)).

For the sources along the array, it can be observed in Figure 4 that the slopes of the P_g branches for all four events are generally linear, both to the north and to the south of each source. The apparent velocities implied by the slopes of the P_g branches are between 5.9 and 6.1 km/s. Modeling of the P_g travel times for these events was first done using an initial 1D crustal model (Fig. 4a, solid line) derived from an average crustal model of [Meissner et al. \(2004\)](#) for the INDEPTH III experiment but with somewhat slower velocities in the mid to lower crust, as inferred by the linear slopes of the observed P_g arrivals for Hi-CLIMB. Fig 4b shows the observed P -wave travel times for the relocated events L2a, L2d, L3a, and L3b compared with the travel times calculated using the initial 1D crustal velocity model. All travel times are reduced by 8.0 km/s and plotted with respect to the minimum recorded travel time rather than an absolute origin time whose precise value is unknown. In Figure 4b,c, the origin position of each event on the x axis is determined by its projected position along the linear trend of the Hi-CLIMB array, shown by the solid line in Figure 1. However, as with the record sections, the P -wave travel times are plotted in either direction away from the source position as a function of epicentral distance from the source to each receiver.

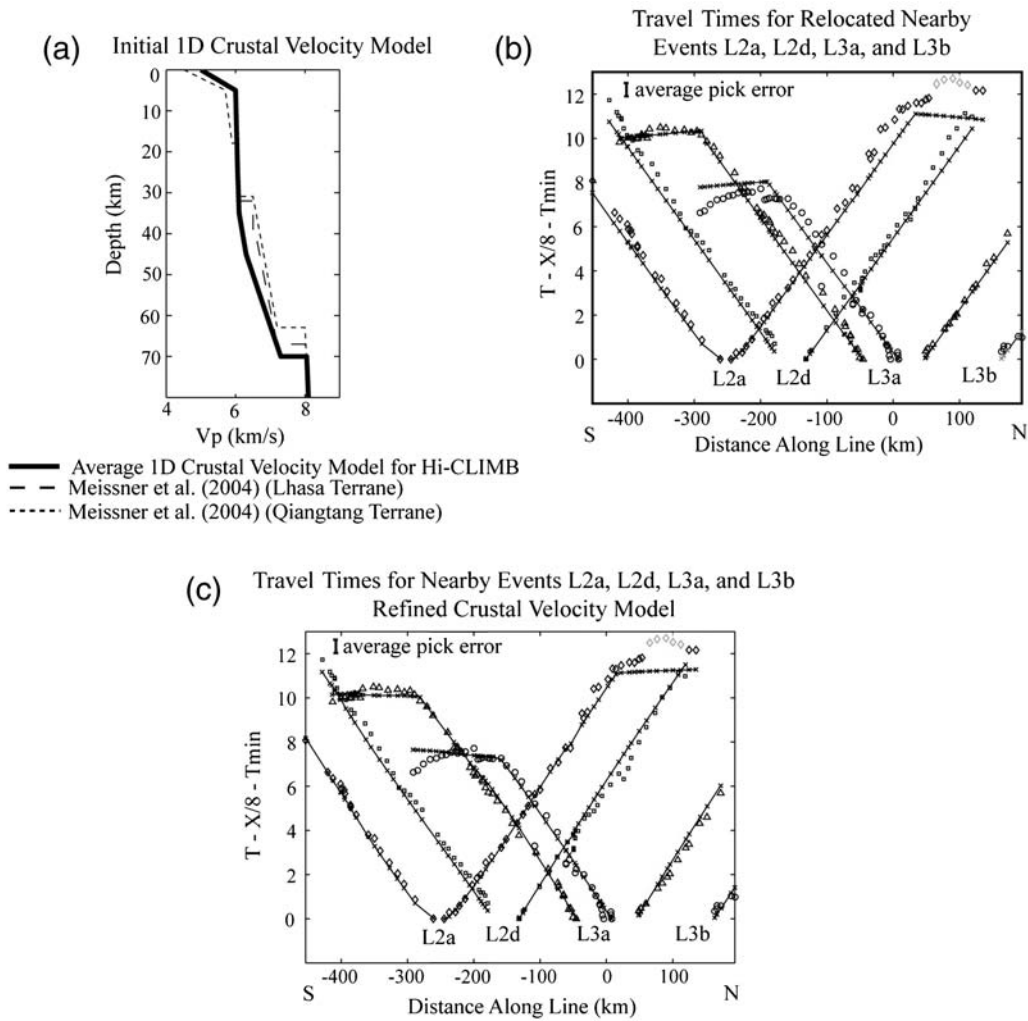


Figure 4. (a) The initial 1D crustal velocity model (solid line) found for the region of Hi-CLIMB with upper crustal velocities similar to those found by Meissner *et al.* (2004) but with slower velocities in the mid to lower crust. (b) The observed travel times of the first arriving P waves for the relocated events L2a (diamonds), L2d (squares), L3a (triangles), and L3b (circles), compared with the calculated travel times (lines and crosses) using the initial 1D crustal velocity model. All travel times are reduced by 8.0 km/s and plotted with respect to the minimum recorded travel time. The origin of each event is placed respective to its projected position along the solid line in Figure 1. (c) The same observations as in (b) but with travel times (lines and crosses) predicted from using a refined crustal velocity model and laterally varying Moho model.

Although the initial 1D crustal velocity model does a reasonable job of fitting the travel times, there are still some mismatches between the observed and calculated travel times. The misfit between the observed and calculated travel times can be seen in Figure 4b for event L2a at distances less than -400 km and greater than -100 km on the x axis, for L2d at distances less than -300 km and greater than $+50$ km on the x axis, and for L3b at distances less than -50 km on the x axis. This indicates that there is some additional lateral variability in the crustal velocities along the profile of the array. Therefore, starting from the initial 1D velocity profile, a refined crustal velocity model was obtained that includes a reduction of up to 0.15 km/s (around 3%) from the initial 1D crustal model in the top 30 km of the crust to the north of latitude 33.5° N and to the south of latitude 31° N.

Figure 4c compares the observed and calculated travel times for the refined crustal velocity model and shows that the reduced velocities beneath the southern and northern portions of the array provide a better fit to the observed travel times at far offsets. The observed Pg travel times for event L3a are well fit by the calculated travel times using the refined crustal velocity model, and the value of rms misfit for the Pg travel times is only 0.25 s, which is smaller than the average picking error. The refined crustal velocity model also produces a good fit between the observed and calculated Pg travel times for event L3b, and the average misfit of Pg arrivals is 0.29 s. For event L2a, the observed Pg travel times at far offsets are well fit by those calculated for the refined crustal velocity model and results in an rms misfit of 0.24 s for crustal arrivals. The observed travel times to the north of event L2d are generally well matched by the calculated travel

times for the refined crustal velocity model, but the observed P_g travel times for stations to the south are still somewhat later than those calculated. Also, the observed travel times of L2d are earlier than those calculated for this model between offsets of 75 to 200 km to the north, which could possibly be due to the presence of a localized zone of high velocity. However this is not observed in the travel times for other sources recorded at the same stations, so, while the average value of rms misfit of 0.43 s is slightly larger than the average picking error, a crustal model that provides a better fit for travel times at these offsets for event L2d would not be consistent with the data observed from the other events. Nonetheless, the refined crustal velocity model provides the best average fit to the P_g travel times for all the events along the array.

While the P_n branches recorded for the nearby events shown in Figure 4 are typically short and have a lower signal-to-noise ratio, the P_g -to- P_n crossover distances can offer some initial constraints on the depth of the Moho along the Hi-CLIMB array. The P_g -to- P_n crossover distances for the events L2a, L3a, and L3b are observed at epicenter distances in the range of 250–300 km and are consistent with crustal thicknesses of up to 73 km in the south beneath event L3a but with a thinner crust to the north beneath event L3b. The Moho depths of the refined crustal velocity model can be constrained by the observed P_g -to- P_n crossover distances of these two events, as well as the observed P_n branches of the more regional events located farther from the array. While not all the observed P_n travel times for event L2a are well fit, there is some uncertainty in the P_n picks for this event, and there is a possibility that these arrivals were picked late or on a different phase. However, this could also result from additional 3D complications in the derived Moho model.

Earthquakes at Far Regional Distances from the Hi-CLIMB Array

Six far regional earthquakes recorded by the Hi-CLIMB array in Tibet were selected to study P_n velocities and Moho depths to determine the velocity structure of the crust and upper mantle in the region. The events shown in Figure 1 were selected because they have prominent P_n arrivals, as well as some P_g arrivals, so that the crossover distance is included. While these events are located too far from the Hi-CLIMB array to be effectively relocated, the depths were estimated to be consistent with the observed P_g -to- P_n crossover distances for each event, and the Moho depths were inferred from the nearby events and the other far regional events (E available as an electronic supplement to this paper; see also Griffin, 2010).

The observed P -wave travel times for the regional earthquakes are shown in Figure 5. In Figure 5a, the observed travel times for event L1e show that the P_g travel times are consistent with the average velocities of around 6.0 km/s inferred from the four events nearby the Hi-CLIMB array. It can be seen that the P_n travel times for stations at distances

between 250 and 450 km are delayed in comparison with those at distances greater than 500 km to the north of the event. Travel-time modeling indicates that the Moho is deeper in the southern portion of the model at a depth of around 73 km and shallower to the north at a depth of around 64 km. The slope of the P_n branch to the south can be modeled by upper-mantle velocities and velocity gradients of around 8.3 km/s and 0.004 s⁻¹, respectively. The slope of the P_n branch to the north can be modeled by upper-mantle velocities and velocity gradients of 7.8 km/s and 0.003 s⁻¹, respectively. The P_n travel-time curve for event L1e shows a transition between 400 and 550 km from the source and indicates that the transition between the deeper Moho in the south and the shallower Moho to the north occurs over a horizontal distance of roughly 150 km between the latitudes of 31° and 32.5° N. The value of the rms misfit between the observed and calculated travel times for this event using the inferred 3D regional velocity model (Figs. 6 and 7) is 0.27 s. Some of the misfit might suggest further complications on the P_n speeds away from the Hi-CLIMB array. However, here a self-consistent velocity model among all the seismic gathers is developed.

Figure 5b shows the observed travel times for event L1a located to the south of the Hi-CLIMB array. As with event L1e, the observed P_g travel times are consistent with the crustal velocities observed using the four nearby events to the Hi-CLIMB array. The observed P_g -to- P_n crossover distance and P_n travel times indicate Moho depths, upper-mantle velocities, and velocity gradients with values in the south and the north similar to those found for event L1e. The P_n travel times are consistent with the northward shallowing of the Moho, occurring over a distance of roughly 150 km between the latitudes 31° and 32.5° N (similar to that found in event L1e).

These results also agree with the data from events L1i, L1j, and L1k with epicenters located near event L1a and are shown in Figures 5c–e. Because these events have similar epicentral locations, they provide a good assessment of the overall data quality. The value of the rms misfit between the observed travel times and the calculated travel times for event L1a using the 3D regional velocity model (Figs. 6 and 7) is 0.16 s, and similar values were found for events L1i, L1j, and L1k.

Event E3b is located to the northeast of the Hi-CLIMB array, and Figure 5f shows the observed travel times for this event. The calculated P_g travel times agree with the observed travel times using the refined crustal velocity model determined from the four events located nearby the array. The observed P_n travel times indicate Moho depths, upper-mantle velocities, and velocity gradients with values in the south and north parts of the model are similar to those found for the other far regional events. However, the transition between P_n travel times in the north and in the south, shown by the bar in Figure 5f, indicates that the Moho shallows northward over a slightly longer distance of around 200 km and slightly farther to the south between the latitudes of 30°

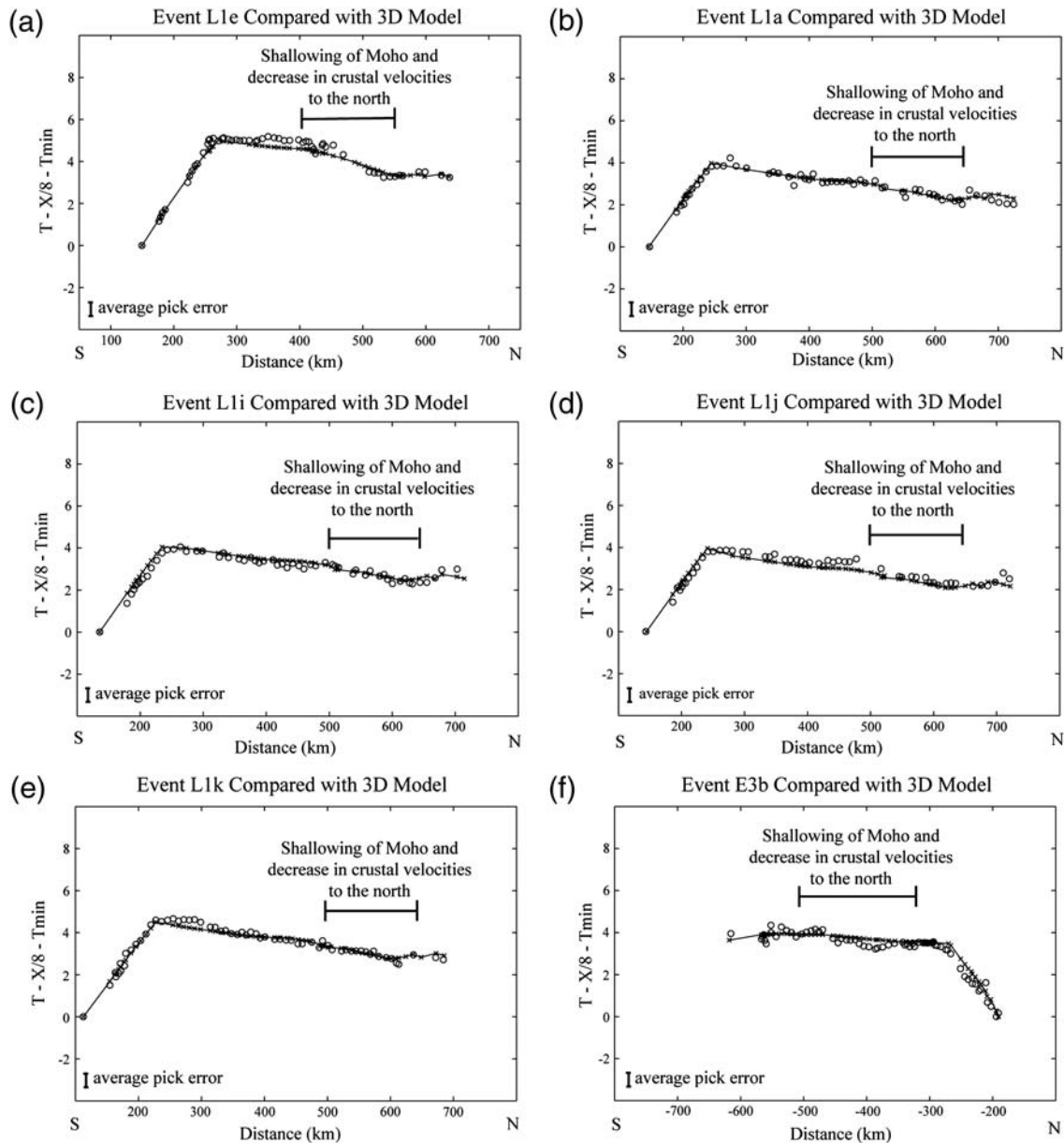


Figure 5. The observed P -wave travel times (circles) for events (a) L1e, (b) L1a, (c) L1i, (d) L1j, (e) L1k, and (f) E3b. These sources are located at regional distances to the Hi-CLIMB array, and P_n travel times for these events were used to constrain the P -wave velocity structure of the upper mantle for the region of the Tibetan plateau. All travel times are reduced by 8.0 km/s and plotted with respect to the minimum recorded travel time. The lines and crosses in each figure show the calculated travel times using the 3D regional velocity model found in this study. Horizontal bars highlight the locations of the transition for shoaling of the Moho and northward decrease in P_n speed.

and 32° N. The regional velocity model determined in this study (Figs. 6 and 7) results in an rms misfit of 0.26 s between the calculated and observed travel times for this event. Some of the misfit could result from additional variations in the P_n velocities at greater distances from the Hi-CLIMB array and also in the vicinity of the transition in Moho depth near the BNS.

Results and Discussion

Using 3D ray tracing (the CRT algorithm, [Cerveny et al., 1988](#)) to forward model the P_g and P_n travel times, we have

determined a 3D P -wave velocity model for the crust and upper mantle in the central and western Tibetan plateau. Figure 6a illustrates the crustal velocities found beneath the Hi-CLIMB array; these crustal velocities vary laterally from north to south and are slightly slower in the areas of the IYS and north of the BNS. Figure 7 highlights the velocity structure of the upper mantle and shows that upper-mantle velocities of around 8.3 km/s and crustal thicknesses of close to 73 km are found beneath the southern portion of the Tibetan plateau. To the north of the BNS in the Qiangtang terrane, upper-mantle velocities are found to be lower, at around

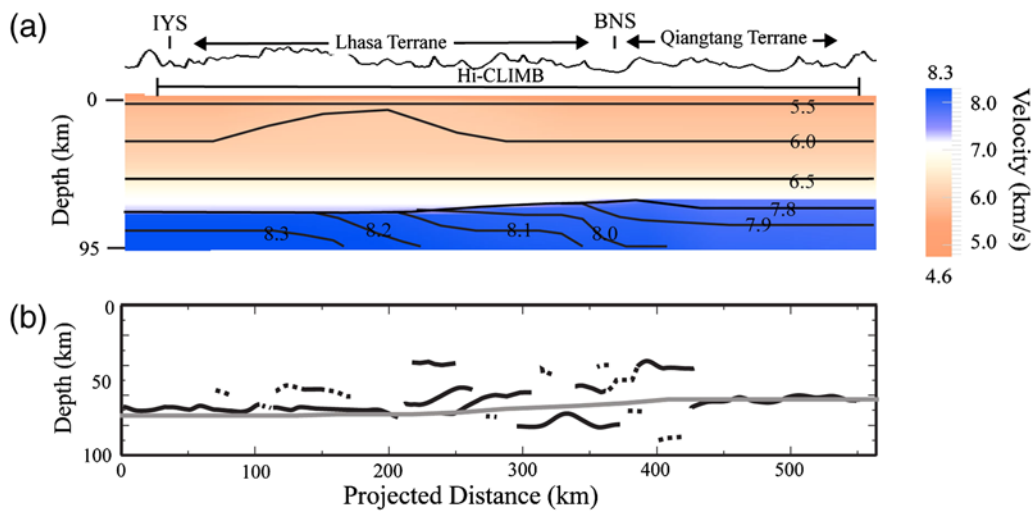


Figure 6. (a) The P -velocity model determined in this study, showing a 2D transect along the strike of the Hi-CLIMB array shown in Figure 1. Solid lines show velocity contours in km/s. Generally, slower crustal velocities were found beneath the areas of the BNS and IYS. Also, a thicker crust and faster upper-mantle velocities were found in the southern area of the plateau beneath the Lhasa terrane. (b) Comparison of the crustal thickness beneath the area of the Hi-CLIMB array determined in this study (gray line) with the interpretation of the major impedance discontinuities (black lines) adapted from the teleseismic imaging by Nowack *et al.* (2010). The color version of this figure is available only in the electronic edition.

7.8 km/s, and the crust in this area is about 10 km thinner than that observed to the south.

The separation between the Lhasa terrane to the south and the Qiangtang terrane to the north can also be observed in receiver function images from Hi-CLIMB (Nabelek *et al.*, 2009; Nowack *et al.*, 2010) as a disruption in the Moho conversion in the receiver function images to the south of the BNS. The location of this disruption coincides with the transition in the Moho depth and upper-mantle velocities found in this study. Figure 6b shows a comparison of the Moho depth results in this study (gray line), from wide-angle travel-time modeling using regional events, with the teleseismic imaging results of Nowack *et al.* (2010), in which the solid lines are the interpreted locations of the subsurface Moho and other major impedance discontinuities. Tseng *et al.* (2009) also determined Moho depths from virtual wide-angle seismic profiles using teleseismic data, and their wide-angle imaging results are consistent with the results of this study. While the results from geologic mapping and balanced cross sections given in Kapp *et al.* (2005) and Ding *et al.* (2007) suggest a northward dipping suture near the surface between the Lhasa and Qiangtang terranes, the results of this and other geophysical studies from Hi-CLIMB (Tseng *et al.*, 2009; Nowack *et al.*, 2010) find a zone of changing Moho depth that suggests a geophysical suture at depth is mainly located to the south of the surface expression of the BNS, which could imply a southward-dipping geophysical suture between the Lhasa and the Qiangtang terranes.

Regional tomography studies have found lower than average P_g and S_g velocities in the Tibetan crust of around 6.1 and 3.4 km/s, respectively (Sun and Toksoz, 2006; Monsalve *et al.*, 2008; Steck *et al.*, 2009). Prior studies using both Hi-CLIMB and INDEPTH III data have also observed

lower-velocity zones in the crust near the areas of the IYS and BNS (Meissner *et al.*, 2004; Hung *et al.*, 2010), which is similar to the results found from this study for the crust. Also, the results for upper mantle P_n velocities found in this study are consistent with earlier studies of P_n in Tibet, including those of Hearn *et al.* (2004), Sun and Toksoz (2006), Liang and Song (2006), and Phillips *et al.* (2007).

The inferred upper-mantle velocities and gradients from this study are consistent with those of Phillips *et al.* (2007) in

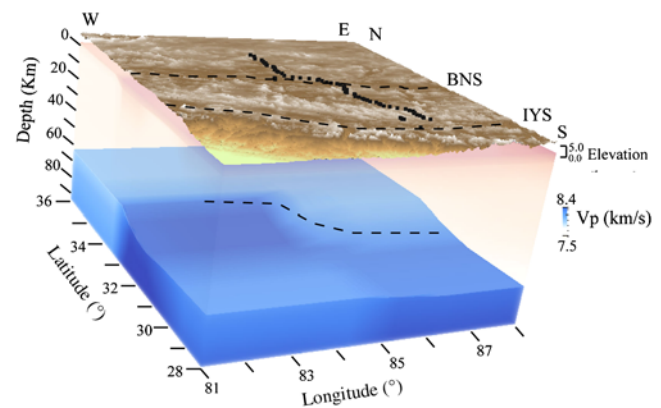


Figure 7. A rendering of the 3D Moho and upper-mantle velocity structure found in this study for the region of the Tibetan Plateau. The upper-mantle velocities are higher and the Moho deeper beneath the southern portion of the plateau south of the BNS, and upper-mantle velocities are lower and the Moho is shallower north of the BNS. However, the area of higher velocities extends farther to the north in the west than in the east and generally follows the trend of the Bangong-Nujiang suture (BNS) as shown by the dashed line along the Moho. The color version of this figure is available only in the electronic edition.

Tibet, with upper-mantle velocity gradients in this region of Tibet between 0.003 s^{-1} and 0.004 s^{-1} . Myers *et al.* (2010) found similar upper-mantle velocity gradients in southern Tibet but lower gradients in the Qiangtang terrane in northern Tibet. However, their study was much larger in scale, incorporating Eurasia and North Africa. For this study, the upper-mantle velocities are well modeled by the regional travel-time data, but the modeled upper-mantle velocity gradients are less constrained (Griffin, 2010). For a better resolution of upper-mantle velocity gradients, longer offsets than those used here would be needed because the offsets in this study were restricted to include only events with well-recorded crossover distances between the P_g and P_n branches. Alternatively, other seismic attributes, such as P_n amplitudes, could be used to provide better constraints on the upper-mantle velocity gradients and are the subject of current research.

Although the event coverage in this study is limited, in addition to the north–south variation, the inferred velocity model also shows an east–west lateral variation. The location and width of the transition in Moho depth is largely constrained by the travel times for ray paths from the regional event L1e (sampling mostly to the west of the Hi-CLIMB array) and the travel times of the ray paths of event E3b (sampling predominantly to the east of the array). To the west, the Moho is found to shallow to the north between the latitudes of 31° and 32.5° N , whereas, to the east, the northward shallowing of the Moho is found to occur farther to the south between 30° and 32° N and generally follows the surface trend of the BNS.

Conclusions

This study uses broadband seismic data recorded by the Hi-CLIMB array in central and western Tibet from earthquake sources located both along the array and at more regional distances from it. These events provide travel-time data along the profile of the array but also afford some azimuthal coverage of the region. Observed P -wave travel times from selected regional earthquakes were modeled using 3D ray tracing in order to determine the velocity structure of the crust and upper-mantle structure in Tibet near the Hi-CLIMB array. Although only a limited number of events were used for the travel-time modeling, the results are consistent with earlier results from teleseismic imaging beneath the Hi-CLIMB array.

A laterally varying refined crustal velocity model was found using P_g travel times from the events located along and near the Hi-CLIMB array, and the inferred velocities are similar to those given by Meissner *et al.* (2004) for INDEPTH III in the upper crust but with slower velocities in the mid to lower crust beneath the Hi-CLIMB array. Crustal velocities in the top 30 km of the crust were also found to be up to 0.15 km/s slower in the area of the IYS south of latitude 31° N and in the area of the BNS north of latitude 33.5° N .

The P_n travel times observed for the more regional events to the Hi-CLIMB array were used to constrain the Moho structure and upper-mantle velocities in the region. It was found that the crust is as thick as 73 km beneath the southern part of the plateau in the Lhasa terrane and about 10 km thinner beneath the northern area of the plateau in the Qiangtang terrane. This north–south variation is also present in the inferred variation in upper-mantle velocities, which were found to be about 8.3 km/s beneath the Lhasa terrane in the southern plateau but as low as 7.8 km/s to the north of the BNS beneath the Qiangtang terrane. However, the travel-time data from events L1e to the west of the Hi-CLIMB array and E3b to the east of the array, imply variations in the east–west direction as well, generally following the surface trend of the BNS. The transition from faster upper-mantle velocities and a thicker crust in the south to slower upper-mantle velocities and a thinner crust in the north occurs over a distance of 150 km between the latitudes of 31° and 32.5° N in the western portion of the velocity model and occurs over a distance of around 200 km between the latitudes of 30° and 32° N in the eastern portion of the model.

Data and Resources

Seismic data used in this study were collected by several authors of this paper as part of the Hi-CLIMB Project using instruments from a number of different sources, including many from the Incorporated Research Institutions in Seismology–Program for the Array Seismic Studies of the Continental Lithosphere (IRIS-PASSCAL) Center. The project was organized and coordinated jointly by the University of Illinois (principal investigator, Wang-Ping Chen) and Oregon State University (principal investigator, John Nabelek). Seismic data is now available directly from the IRIS Data Management Center at www.iris.edu.

Ray tracing was performed using the 3D ray-tracing code by Cerveny *et al.* (1988; the CRT algorithm, available at <http://sw3d.mff.cuni.cz>), and event relocation was performed using the location code HYPOINVERSE-2000 (Klein, 2002; available at <http://earthquake.usgs.gov/research/software>).

The U.S. Geological Survey/National Earthquake Information Center earthquake locations are available at <http://earthquake.usgs.gov/earthquakes/eqarchives/epic/database.php> (last accessed, November 2010). The Engdahl–van der Hilst–Buland catalog of earthquakes (Engdahl *et al.*, 1998) is available at <http://www.isc.ac.uk/search/bulletin/ehb.html> (last accessed October 2010).

Acknowledgments

This work was supported by the U.S. National Science Foundation grants EAR06-35419 (W. P.C., T.-L. T.), EAR06-35611 (R.L.N.), and the U.S. Air Force AFRL grant FA8718-08-C-002 (J.D.G., R.L.N., W.-P.C. and T.-L. T.).

References

- Barazangi, M., and J. Ni (1982). Velocities and propagation characteristics of P_n and S_n beneath the Himalayan arc and Tibetan plateau: Evidence for underthrusting of Indian continental lithosphere beneath Tibet, *Geology* **10**, 179–185.
- Barron, J., and K. Priestley (2009). Observations of frequency-dependent S_n propagation in northern Tibet, *Geophys. J. Int.* **179**, 475–488.
- Brandon, C., and B. Romanowicz (1986). A no-lid zone in the central Chang-Thing platform of Tibet—Evidence from pure path phase-velocity measurements of long period Rayleigh waves, *J. Geophys. Res.* **91**, 6547–6564.
- Cerveny, V., L. Klimes, and I. Psencik (1988). Complete seismic-ray tracing in three-dimensional structures, in *Seismological Algorithms*, D. J. Doornbos (Editor), Academic Press, London, 89–168.
- Chen, W.-P., and P. Molnar (1981). Constraints on the seismic wave velocity structure beneath the Tibetan plateau and their tectonic implications, *J. Geophys. Res.* **86**, 5937–5962.
- Chen, W.-P., and P. Molnar (1983). Focal depths of intracontinental and intraplate earthquakes and their implications for the thermal and mechanical properties of the lithosphere, *J. Geophys. Res.* **88**, 4183–4214.
- De la Torre, T. L., G. Monsalve, A. F. Sheehan, S. Sapkota, and F. Wu (2007). Earthquake processes of the Himalayan collision zone in eastern Nepal and the southern Tibetan plateau, *Geophys. J. Int.* **171**, 718–738.
- Dewey, J. F., R. M. Shackleton, C. Chengfa, and S. Yiyin (1988). The tectonic evolution of the Tibetan plateau, *Phil. Trans. Roy. Soc. London Ser. A*, **327**, 379–413.
- Ding, L., P. Kapp, Y. Yue, and Q. Lai (2007). Postcollisional calc-alkaline lavas and xenoliths from the southern Qiangtang terrane, central Tibet, *Earth Planet. Sci. Lett.* **254**, 28–38.
- Engdahl, E. R., R. van der Hilst, and R. Buland (1998). Global teleseismic earthquake relocation with improved travel times and procedures for depth determination, *Bull. Seismol. Soc. Am.* **88**, 722–743.
- Griffin, J. D. (2010). Modeling of three-dimensional regional velocity structure using wide angle seismic data from the Hi-CLIMB experiment in Tibet, *M.S. Thesis*, Purdue University, West Lafayette, Indiana, 102 pp.
- Haines, S. S., S. L. Klemperer, L. Brown, G. Jingru, J. Mechie, R. Meissner, A. Ross, and Z. Wenjin (2003). INDEPTH III seismic data: from surface observations to deep crustal processes in Tibet, *Tectonics* **22**, doi 10.1029/2001TC001305.
- Hearn, T. M., S. Wang, J. F. Ni, Z. Xu, Y. Yu, and X. Zhang (2004). Uppermost mantle velocities beneath China and surrounding regions, *J. Geophys. Res.* **109**, no. B11301, doi 10.1029/2003JB002874.
- Hirn, A., A. Necessian, M. Sapin, G. Jobert, Z. X. Xu, E. Y. Gao, D. Y. Lu, and J. W. Teng (1984). Lhasa block and bordering sutures—A continuation of a 500 km Moho traverse through Tibet, *Nature* **307**, 25–27.
- Hung, S.-H., W.-P. Chen, L.-Y. Chiao, and T.-L. Tseng (2010). First multi-scale, finite-frequency tomography illuminates 3-D anatomy of the Tibetan plateau, *Geophys. Res. Lett.* **37**, L06304, doi 10.1029/2009GL041875.
- Jimenez-Munt, I., M. Fernandez, J. Verges, and J. P. Platt (2008). Lithosphere structure underneath the Tibetan plateau inferred from elevation, gravity and geoid anomalies, *Earth Planet. Sci. Lett.* **267**, 276–289.
- Kapp, P., A. Yin, T. M. Harrison, and L. Ding (2005). Cretaceous-Tertiary shortening, basin development and volcanism in central Tibet, *Geol. Soc. Am. Bull.* **117**, 865–878.
- Kind, R., X. Yuan, J. Saul, D. Nelson, S. V. Sobolev, J. Mechie, W. Zhao, G. Kosarev, J. Ni, U. Achauer, and M. Jiang (2002). Seismic images of crust and upper mantle beneath Tibet: Evidence for Eurasian plate subduction, *Science* **298**, 1219–1221.
- Klein, F. (2002). HYPOINVERSE-2000 (version 4/2002). U.S. Geological Survey, Menlo Park, California.
- Liang, C., and X. Song (2006). A low velocity belt beneath northern and eastern Tibetan plateau from P_n tomography, *Geophys. Res. Lett.* **33**, L22306, doi 10.1029/2006GL027926.
- Liang, C., X. Song, and J. L. Huang (2004). Tomographic inversion of P_n travel times in China, *J. Geophys. Res.* **109**, no. B11304, doi 10.1029/2003JB002789.
- McNamara, D. E., T. J. Owens, P. G. Silver, and F. T. Wu (1994). Shear-wave anisotropy beneath the Tibetan plateau, *J. Geophys. Res.* **99**, 13,655–13,665.
- McNamara, D. E., T. J. Owens, and W. R. Walter (1995). Observations of regional phase propagation across the Tibetan plateau, *Geophys. Res. Lett.* **100**, 22,215–22,219.
- McNamara, D. E., W. R. Walter, T. J. Owens, and C. J. Ammon (1997). Upper mantle velocity structure beneath the Tibetan plateau from P_n travel time tomography, *J. Geophys. Res.* **102**, 493–505.
- Meissner, R., F. Tilmann, and S. Haines (2004). About the lithospheric structure of central Tibet, based on seismic data from the INDEPTH III profile, *Tectonophysics* **380**, 1–25.
- Molnar, P., and P. Tapponnier (1975). Cenozoic tectonics of Asia—Effects of a continental collision, *Science* **189**, 419–426.
- Monsalve, G., A. Sheehan, C. Rowe, and S. Rajauri (2008). Seismic structure of the crust and the upper mantle beneath the Himalayas: Evidence for eclogitization of lower crustal rocks in the Indian plate, *J. Geophys. Res.* **113**, no. B08315.
- Myers, S. C., M. L. Begnaud, S. Ballard, M. E. Pasyanos, W. S. Phillips, A. L. Ramirez, M. S. Antolik, K. D. Hutchenson, J. J. Dwyer, C. A. Rowe, and G. S. Wagner (2010). A crust and upper-mantle model of Eurasia and North Africa for P_n travel time calculation, *Bull. Seismol. Soc. Am.* **100**, 640–656.
- Nabelek, J., W.-P. Chen, M. R. Pandey, J. Mei, J. Chen, and B. S. Huang The Project Hi-CLIMB Team (2005). Hi-CLIMB : A high-resolution seismic profile across the Himalayas and southern Tibet, Annual Report, Incorporated Research Institutions for Seismology, Washington D.C., 1371–1374, doi 10.1126/science.1167719.
- Nabelek, J., G. Hetenyi, J. Vergne, S. Sapkota, B. Kafle, M. Jian, H. Su, J. Chen, and B. S. Huang (2009). Underplating in the Himalaya-Tibet collision zone revealed by the Hi-CLIMB experiment, *Science* **325**, 1371–1374.
- Ni, J., and M. Barazangi (1983). High-frequency seismic wave propagation beneath the Indian shield, Himalyan arc, Tibetan plateau and surrounding regions: High uppermost mantle velocities and efficient S_n propagation beneath Tibet, *Geophys. J. Roy. Astron. Soc.* **72**, 665–689.
- Nowack, R. L., W.-P. Chen, and T.-L. Tseng (2010). Application of Gaussian beam migration to multi-scale imaging of the lithosphere beneath the Hi-CLIMB array in Tibet, *Bull. Seismol. Soc. Am.* **100**, 1743–1754.
- Pei, S., J. Zhao, Y. Sun, X. Xu, S. Wang, H. Liu, C. A. Rowe, M. N. Toksoz, and X. Gao (2007). Upper mantle seismic velocities and anisotropy in China Determined through P_n and S_n tomography, *J. Geophys. Res.* **112**, no. B05312, doi 10.1029/2006JB004409.
- Phillips, W. S., M. L. Begnaud, C. A. Rowe, L. K. Steck, S. C. Myers, M. E. Pasyanos, and S. Ballard (2007). Accounting for lateral variations of the upper mantle gradient in P_n tomography studies, *Geophys. Res. Lett.* **34**, L14312, doi 10.1029/2007GL029338.
- Shi, D., W. Zhao, L. Brown, D. Nelson, X. Zhao, J. Ni, J. Xiong, J. Mechie, J. Guo, S. Klemperer, and T. Hearn (2004). Detection of southward intracontinental subduction of Tibetan lithosphere along the Bangong-Nujiang suture by P -to- S converted waves, *Geology* **32**, 209–212.
- Steck, L. K., W. S. Phillips, K. Mackey, M. L. Begnaud, R. J. Stead, and C. A. Rowe (2009). Seismic tomography of crustal P and S across Eurasia, *Geophys. J. Int.* **177**, 81–92.
- Sun, Y., and M. N. Toksoz (2006). Crustal structure of China and surrounding regions from P wave traveltome tomography, *J. Geophys. Res.* **111**, no. B03310, doi 10.1029/2005JB003962.
- Tapponnier, P., Z. Q. Xu, F. Roger, B. Meyer, N. Arnaud, G. Wittlinger, and J. S. Yang (2001). Geology—Oblique stepwise rise and growth of the Tibetan plateau, *Science* **294**, 1671–1677.

- Tian, X., Q. Wu, Z. Zhang, J. Teng, and R. Zeng (2005). Joint imaging by teleseismic converted and multiple waves and its application in the INDEPTH-III passive seismic array, *Geophys. Res. Lett.* **32**, L21315, doi [10.1029/2005GL023686](https://doi.org/10.1029/2005GL023686).
- Tilmann, F., J. Ni, and The INDEPTH III Seismic Team (2003). Seismic imaging of the downwelling Indian lithosphere beneath central Tibet, *Science* **300**, 1424–1427.
- Tseng, T.-L., W.-P. Chen, and R. L. Nowack (2009). Northward thinning of Tibetan crust revealed by virtual seismic profiles, *Geophys. Res. Lett.* **36**, L24304, doi [10.1029/2009GL040457](https://doi.org/10.1029/2009GL040457).
- Wittlinger, G., V. Farra, G. Hetenyi, J. Vergne, and J. Nabelek (2009). Seismic velocities in southern Tibet lower crust: A receiver function approach for eclogite detection, *Geophys. J. Int.* **177**, 1037–1049.
- Wittlinger, G., V. Farra, and J. Vergne (2004). Lithospheric and upper mantle stratifications beneath Tibet: New insights from S_p conversions, *Geophys. Res. Lett.* **31**, L19615, doi [10.1029/2004GL020955](https://doi.org/10.1029/2004GL020955).
- Xie, J., R. Gok, J. Ni, and Y. Aoki (2004). Lateral variations of crustal seismic attenuation along the INDEPTH profiles in Tibet from L_g Q inversion, *J. Geophys. Res.* **109**, no. B10308, doi [10.1029/2004JB002988](https://doi.org/10.1029/2004JB002988).
- Yin, A., and T. M. Harrison (2000). Geologic evolution of the Himalayan-Tibetan orogen, *Ann. Rev. Earth Planet Sci.* **28**, 211–280.
- Zhao, W. J., K. D. Nelson, and The INDEPTH Seismic Team (1993). Deep seismic-reflection evidence for continental underthrusting beneath southern Tibet, *Nature* **366**, 557–559.
- Zhao, W., J. Mechie, L. D. Brown, J. Guo, S. Haines, T. Hearn, S. L. Klemperer, Y. S. Ma, R. Meissner, K. D. Nelson, J. F. Ni, P. Pananont, R. Rapine, A. Ross, and J. Saul (2001). Crustal structure of central Tibet as derived from Project INDEPTH III wide-angle seismic data, *Geophys. J. Int.* **145**, 486–498.

Department of Earth and Atmospheric Sciences
Purdue University
West Lafayette, Indiana 47907
jessdgriffin@gmail.com
(J.D.G., R.L.N.)

Department of Geology
University of Illinois-Urbana
Urbana, Illinois 61801
(W.-P.C., T.-L.T.)

Manuscript received 24 August 2010